J Mater Sci: Mater Electron (2021) 32:10927–10942

Novel$Al_{1.997}Hf_{0.003}O_3$ High-*k* gate dielectric thin films grown by pulsed laser deposition usingpre-synthesized target material

Annie Maria Mahat[1,2,*], Mohd Sufri Mastuli[1,2], Nurhanna Badar[3], and Norlida Kamarulzaman[1,2]

[1] Center for Functional Materials and Nanotechnology, Institute of Science, Universiti Teknologi MARA, 40450 Shah Alam, Selangor, Malaysia
[2] Faculty of Applied Sciences, Universiti Teknologi MARA, 40450 Shah Alam, Selangor, Malaysia
[3] Faculty of Science and Marine Environment, Universiti Malaysia Terengganu, 21030 Kuala Nerus, Terengganu, Malaysia

Received: 14 December 2020
Accepted: 11 March 2021
Published online:
29 March 2021

© Springer Science+Business Media, LLC, part of Springer Nature 2021

ABSTRACT

The present study reported pure pre-synthesized $Al_{1.997}Hf_{0.003}O_3$ target for the formation of novel high-*k* gate dielectric thin films using pulsed laser deposition technique. High substrate temperature of 800 °C and ultra-high-vacuum condition at 10^{-8} Torr were used to produce stable hexagonal crystal structure of thin films with exclusive crystal growth directions in the (110) and (024) planes as evidenced by the XRD. AFM images displayed dense and uniform distribution of crystallites with RMS as low as 0.12 nm, contributing to very smooth morphology. Optical observation by the UV–Vis analysis showed that the introduction of Hf in the lattice of the Al_2O_3 material had significantly modified the energy bands of $Al_{1.997}Hf_{0.003}O_3$, hence, improved *k* values. Consequently, the C–V measurements of the fabricated thin films based on Pt/$Al_{1.997}Hf_{0.003}O_3$/p-Si MOS capacitor exhibited a high capacitance of ~ 202 nF at ~ 6 nm thickness and attributed to high-*k* value of ~ 21. The *I*–*V* measurements also revealed the electron tunnelling was reduced with thicker films of $Al_{1.997}Hf_{0.003}O_3$, due to this, leakage current density was improved to ~ 10^{-10} A/cm^2. These results revealed that $Al_{2-x}Hf_xO_3$ thin films could be significant in searching for a replacement dielectric for nanoscale MOS devices.

1 Introduction

Developments of new gate oxide for metal–oxide–semiconductor (MOS) applications are important as problems arise with SiO_2 downscaling. Influenced by Moore's law, SiO_2 has served the MOS system for more than five decades [1–10], ever since, SiO_2–Si technology continuously improved and in the domain of digital logic integrated circuits (ICs), was never seriously challenged by any other material

Address correspondence to E-mail: anniemaria@uitm.edu.my; ammahat@gmail.com

https://doi.org/10.1007/s10854-021-05751-7

systems. To comply with Moore's law, the transistor constituents of ICs become smaller and faster to support the growing number of transistors on the ICs [11]. To increase the number of transistors on a microchip, the thickness of the SiO_2 layers must be decreased. In a scaled chip of less than 45 nm, the SiO_2 thickness must be less than 1 nm. This results in high leakage current due to the quantum tunnelling effects [12–15], exceeding the 1 A cm^{-2} gate limit. Thus, for downscaling of the gate oxide to less than 1 nm, SiO_2 is not suitable. Evidently, the number of transistors growth was seen to slow down and become obsolete starting 2013. To keep Moore's Law rolling forward, the replacement of SiO_2 with new gate oxide is necessary.

The best candidates to replace SiO_2 gate oxide will be the high-*k* dielectric materials. High-*k* dielectric materials are materials with high dielectric constant (*k*) as compared to SiO_2 [16]. The principal motivation to use the high-*k* dielectrics is to reduce the direct tunnelling gate leakage currents. When the relative permittivity of an insulator is high, it will increase the amount of capacitance within MOS despite reducing its thickness. For instance, SiO_2 would have a higher capacitance if only its thickness is reduced as its static *k* is only 3.9. Meanwhile, at relatively same amount of capacitance, high-*k* dielectrics still have a long way to go for further scaling. Besides, it will give higher capacitance thus increasing the MOS device performance and significantly reducing gate leakage. However, the choices of high-*k* do not solely depend on its dielectric permittivity, it also requires a wide bandgap.

High-*k* material such as Al_2O_3 has been considered as a potential gate oxide for continuous miniaturization of MOS devices [17, 18]. Al_2O_3 has attracted attention of researchers in the past few decades because of its advantage of being a thermodynamically stable material which is imperative in the compatibility with Si processing. Additionally, Al_2O_3 has a high bandgap of 8.8 eV (conventional value) and *k* value of 9 which is much larger than that of SiO_2 (3.9). However, for future MOS technology endeavour, Al_2O_3 is considered to have a rather low-*k* value. The oxide's *k* value must be over 12 but preferably not more than 25, because *k* value varies inversely with bandgap [19, 20]. The bandgap of materials for MOS technology should be high, of more than 5.8 eV [21].

Over the last decades, HfO_2 has emerged as the designated gate oxide for current MOS technology due to its high-*k* value (25). However, it is still far from being an ideal material. It has a low crystallization temperature and more seriously, it has a low bandgap of 5.1 eV [11, 22–25]. Due to these, study toward potential gate oxide has progressed from single metal oxide to doped oxides. The perspective is to associate the favourable properties of metal oxides while suppressing their disadvantages. Considering these, we studied the substitutional Hf-doped Al_2O_3 materials to engineer the properties of the materials in term of their structure, thermal stability, and bandgap. In our previous works [26, 27], novel $Al_{2-x}Hf_xO_3$ materials have been successfully obtained *via* a combustion synthesis method. $Al_{2-x}Hf_xO_3$ materials exhibited bandgap narrowing with respect to pure Al_2O_3 materials and it is dependent on the Hf content following an exponential function. The inclusion of Hf into the lattice of Al_2O_3 narrowed the bandgap (from 6.09 to 5.86 eV) due to the introduction of donor energy levels. As a result, $Al_{2-x}Hf_xO_3$ were found to have a higher bandgap than HfO_2. The best bandgap value (5.86 eV) which was attributed to improved *k* value was obtained for $Al_{2-x}Hf_xO_3$ at $x = 0.003$. Thus, it is best to study the thin film properties of $Al_{2-x}Hf_xO_3$ at $x = 0.003$. In continuation of the studies, for the first time, this work utilized highly pure pre-synthesized $Al_{2-x}Hf_xO_3$ ($x = 0.003$) as a target to deposit $Al_{1.997}Hf_{0.003}O_3$ thin films using an appropriate deposition technique. Commonly, a commercial target is used to deposit metal oxide thin film. Otherwise, in this work, a highly pure synthesized target was used instead.

The deposition of thin films, especially using new modified materials is different. Problem related to the quality of thin films such as roughness, denseness and non-uniformity is common. These will affect the functional characteristics of the films. Furthermore, when the target is prepared from pure synthesized materials, it is vital to choose the right deposition technique so that the stoichiometry of the materials will not be altered during the process. Sustaining the stoichiometry of the materials in the deposited films is important for reaching the hypothesis made based on the performance of the materials beforehand. As an established technique in physical deposition techniques, pulsed laser deposition (PLD) able to retain the stoichiometry of the materials from the target in the deposited thin films [28–30]. PLD is

considered a clean process where a laser is used as an external energy source without filaments. The laser creates a plume of the to-be deposited material which is then targeted onto a substrate. During the process, PLD also enables the controlling of porosity through partial pressure. As a result, dense and high oriented growth of deposited thin films can be formed. The highly dense and oriented growth of metal oxide thin films is greatly demanded in the semiconductor industry to enhance the electron transport in semiconductor materials. Furthermore, PLD is known to have high deposition rates which is very effective; typically ~ 100 s Å/min can be achieved at moderate laser fluences, with film thickness controlled by the laser shots [31].

Herein, by controlling the parameters (i.e. laser shots, background pressure and substrate temperature), Al_2O_3 and novel $Al_{1.997}Hf_{0.003}O_3$ thin films were deposited at various thicknesses using the PLD technique. Addressing the issue of scaling down, the effect of thickness on the properties of Al_2O_3 and $Al_{1.997}Hf_{0.003}O_3$ thin films such as structure, morphology, optical and electrical were investigated. The electrical measurements of current–voltage (*I–V*) and capacitance–voltage (*C–V*) are based on the Pt/Al_2O_3/p-Si/Pt and Pt/$Al_{1.997}Hf_{0.003}O_3$/p-Si/Pt MOS capacitors. The fabrication of the MOS capacitor is imperative to show the significance and suitability of $Al_{1.997}Hf_{0.003}O_3$ gate oxide thin films for the next generation MOS devices.

2 Experimental

The synthesis of Al_2O_3 and $Al_{2-x}Hf_xO_3$ materials was done using the self-propagating combustion (SPC) method as reported previously [26, 27]. The optimized $Al_{1.997}Hf_{0.003}O_3$ material was used as pre-synthesized target for PLD in this work. Al_2O_3 was treated as a reference sample. The powder materials of Al_2O_3 and $Al_{1.997}Hf_{0.003}O_3$ were compacted into cylindrical discs (referred as targets) by pressing. The compaction was done slowly to facilitate the escape of the entrapped air. The powders were poured into a rigid rust-free die and plunger and press by the single punch compressing machine. The diameter of the pressed powders was 2.0 cm relying on the inner diameter of the die. The thickness of the target varies upon the amount of the powders used and the force applied. The force was varied from 10 to 20 tonne to press the targets. The thickness of the targets ranges from 0.3 to 0.5 cm. The thin films were deposited on p-Silicon (100) substrate using PLD. Any chemical contamination may ruin the entire device performance and reliability; hence, wafer substrate cleaning was implemented. Prior to depositions, substrates were cleaned by standard cleaning procedure that was done on the wet bench. The substrate was immersed in the buffered oxide etch (BOE) solution (1 part HF : 10 parts NH_4F). During rinsing with running deionized (DI) water, DI water wetting/sheeting on the front and back surface of the wafer were observed as SiO_2 is hydrophilic, while Si is hydrophobic. When the hydrophilic condition still appears on the wafer, the wafer was immersed back into the BOE and was rinsed under running DI water until the hydrophobic condition appeared on the wafer. The hydrophobic condition dictates that the wafer was cleaned from any contamination including SiO_2. Then the cleaned wafer was dried under nitrogen air before loading into the PLD chamber.

The films were prepared using the PLD system from Neocera with Compex Pro 102 F KrF excimer laser (λ = 248 nm). A 20 ns pulse duration at 10 Hz repetition rate was utilized. The laser was focussed on the rotating targets to a 4 mm^2 spot corresponding to a fluence of 2.5 J/cm^2. The targets of Al_2O_3 and $Al_{1.997}Hf_{0.003}O_3$ were placed inside the chamber at a 7.5 cm distance from the substrate. Depositions were performed in an ultra-high-vacuum chamber at 4.10×10^{-8} Torr. The number of pulses was varied at 5000, 10,000 and 20,000 for Al_2O_3 thin films with sample identification A5, A10 and A20, respectively. The same goes for $Al_{1.997}Hf_{0.003}O_3$ thin films. All sample were identified as AH5, AH10 and AH20, respectively. No oxygen or other gases were fed into the chamber to ensure the background pressure stayed in the vacuum condition.

The structure of the thin samples was studied by the Grazing Incidence Diffraction (GID) technique in the X-Ray diffractometer (Bruker D8 Advance–Davinci) with Cu Kα radiation. Study toward surface microstructure of the thin films was done using Scanning Probe Microscope (SPM) with SmartSPM-1000. Field Emission Scanning Electron Microscope (FESEM) of JEOL JSM-7600 F was used to observe the thickness of the films. UV–Vis NIR spectrophotometer (Perkin-Elmer Lambda 950) was used to acquire the absorption spectra of all the samples to determine their bandgap energies.

The metal–oxide–semiconductor (MOS) structure for Al_2O_3 and $Al_{1.997}Hf_{0.003}O_3$ gate oxides were fabricated with the configuration Pt/Al_2O_3/p-Si and of Pt/$Al_{1.997}Hf_{0.003}O_3$/p-Si, respectively. The Al_2O_3 and $Al_{1.997}Hf_{0.003}O_3$ thin films were deposited on to p-Si substrate with a resistivity of 2–5 Ω/cm. Further, to form a gate metal electrode, 85-nm-thick platinum film was sputtered by JEOL JFC-1500 Auto Fine Coater using a shadow mask of an area 7.1×10^{-2} cm^2. The same thickness of the platinum film was also sputtered on the backside of the p-Si substrate to ensure an Ohmic contact. The electrical behaviour of the fabricated MOS was determined using Keithley 4200 Semiconductor Characterization Unit for *I–V* and *C–V* measurements in the range of − 4 to + 4 V. For *C–V* measurement, the frequency was set at 1 MHz to determine the dielectric constant of the films. The measurements were done in a full shielded dark chamber at room temperature.

3 Results and discussion

The XRD patterns of all Al_2O_3 and $Al_{1.997}Hf_{0.003}O_3$ films with sample identification A and AH, respectively, are shown in Fig. 1 The XRD patterns are obtained using the GID technique. The advantage of the GID technique is that the X-Ray beam is optically adjusted to graze the thin film part only and XRD patterns will show results of the thin film sample without any contribution from the substrate. Due to small amounts of sample material deposited in the thin films, the inclusion of the substrate peaks will normally overwhelm the thin film sample peaks which will cause the smaller peaks to be suppressed and become unobservable. Hence, it is imperative to employ the right diffraction technique when studying ultra-thin films of less than 100 nm. It is observed that, the acquired XRD patterns are all indexed to the ICDD reference pattern number 01-088-0826 for Al_2O_3 hexagonal structure with space group R-3c as shown in Fig. 1g. This is as expected as the compacted targets used to fabricate the thin films *via* the PLD technique are of the hexagonal crystal structure. Hence, the Al_2O_3 and $Al_{1.997}Hf_{0.003}O_3$ films formed will be of the stable hexagonal crystal structure even though the substrate temperature was 800 °C during the deposition process. It is to be noted that the source targets have been prepared from the highly stable annealed powders from our previous reports

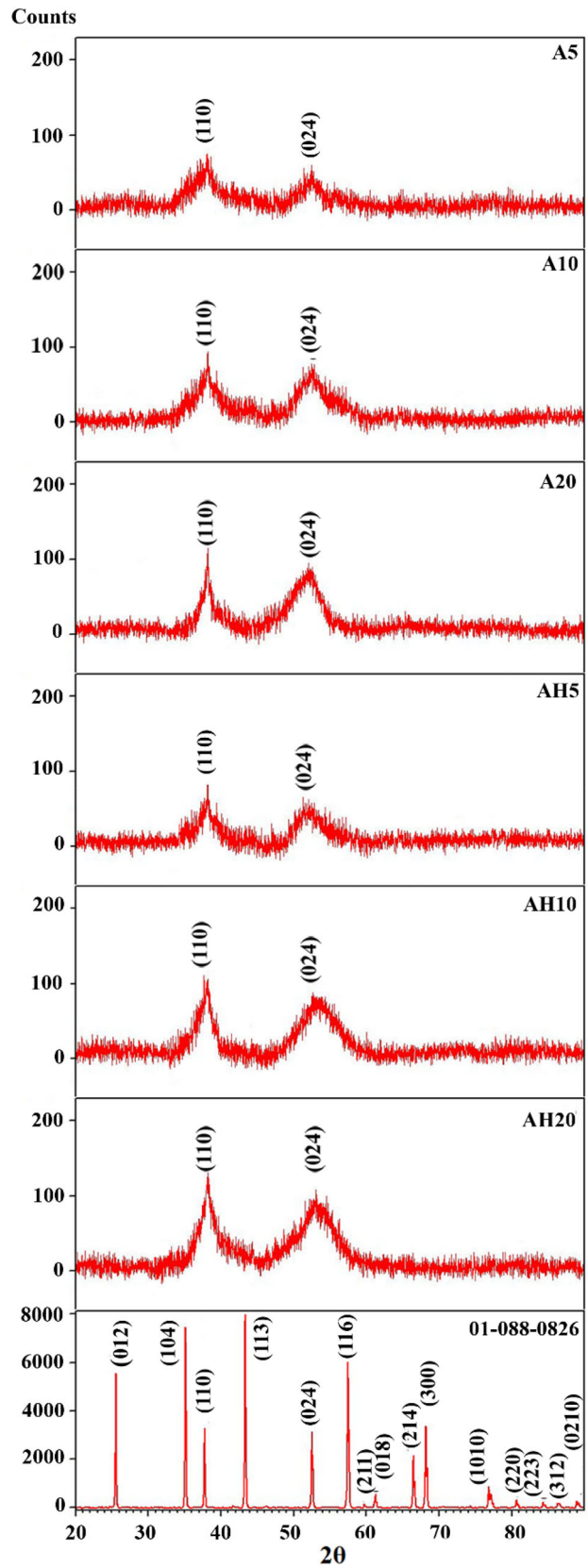

◀**Fig. 1** XRD patterns obtained *via* GID for all Al_2O_3 and $Al_{1.997}Hf_{0.003}O_3$ films with reference pattern of $\alpha-Al_2O_3$

[26, 27]. The diffraction from a crystal specimen produces a peak with a certain width. This is known as peak broadening. The peak width depends on the size of the crystals. Peak width is inversely related to crystal size; that is, peak width increases with decreasing crystal particle size. Hence, the broadness of the XRD peaks show that the crystallites formed on the substrates must be very small resulting in smooth thin film surface as illustrated in the SPM results discussed later.

The thin films that were deposited in a vacuum environment are found to be polycrystalline with highly oriented growth in specific directions of the crystal plane. The direction of the crystal plane for all the films shows exclusive crystal growth in the (110) and (024) directions. It is believed that the vacuum pressure may affect crystal growth direction. For the vacuum environment, the (024) crystal plane can be obtained at a pressure range of 10^{-6} to 10^{-4} Torr as reported by Wang et al. [32] which is also true as shown in these results. The film thickness relies on the number of laser shots [28, 31]. Thus, it is expected that film A20 is thicker than A10, and A5 is the thinnest; the same case implies for AH20, AH10 and AH5 films. It is also observed that as the film thickness decreases the 2θ positions shift to the right meaning that the d-spacing of (110) and (024) crystal planes decrease when the thickness of the samples decreases. This is true for both samples of Al_2O_3 and $Al_{1.997}Hf_{0.003}O_3$. Hence, the d-spacing of the (110) and (024) planes decrease for thinner Al_2O_3 and $Al_{1.997}Hf_{0.003}O_3$ films as shown in Table 1. As such, for deposition conditions used in the thin film fabrication, the crystal growth orientation of the thin films occurred in the (110) and (024) crystal direction.

The AFM 3D images of all the deposited Al_2O_3 and $Al_{1.997}Hf_{0.003}O_3$ films at different thicknesses are shown in Fig. 2. At the typical scan area of $2 \times 2\ \mu m^2$, the AFM images show a dense, uniform distribution of crystallites with very smooth morphology that is believed to be attributed to a high substrate temperature of 800 °C. Zhao et al. [29] reported that high substrate temperature will enhance the crystallinity and produce very smooth and dense films. High substrate temperature will also produce strong interface bonding between the oxide layer and substrate, resulting in the enhanced intensity of thin film oxides with their substrates. This will influence the electrical properties of the MOS capacitor as described in the *I–V* and *C–V* results discussed later. As shown in Table 2, the RMS surface roughness for the Al_2O_3 thin films are 0.27 nm, 0.21 nm and 0.10 nm for A20, A10 and A5 films, respectively. For AH20, AH10 and AH5 films, the RMS are 0.30 nm, 0.23 nm, and 0.12 nm, respectively. It is observed that the decrease in the thickness of films produces a decrease in surface roughness which agrees well to Gao et al. [33]. It is observed that thinner films are smoother compared to thicker ones attributed to the increased crystal defects where increased numbers of laser shots are needed to form thicker films. These results agree well with results from Kamarulzaman et al., Badar et al., and Yang et al. [31, 34, 35] where the films obtained are smooth and dense with no pinholes or voids. It is evidence that the quality of the thin films obtained from PLD is very high in terms of smoothness and uniformity of thickness, that is, of the order of about a tenth of a nanometer. Figure 3 shows the cross-sections of the thin films obtained *via* FESEM. It is observed that the thicknesses of the thin films are between 6.56 and 21.36 nm. It is evident here that the thickness is dependent on the number of laser shots. The thin films obtained here are thinner than those from Kamarulzaman et al. [31] with a similar number of laser shots due to higher vacuum background pressure (pressure used here is of 10^{-8} Torr, whereas the value for N. Kamarulzaman was of 10^{-7} Torr). From the SEM cross-sections of the thin films, it is obvious that PLD can produce very high-quality uniform thin films that are very smooth.

Table 1 d-spacings of Al_2O_3 and $Al_{1.997}Hf_{0.003}O_3$ thin film samples from GID

Samples	GID	
	(110) ± 0.0001	(024) ± 0.0001
Al_2O_3 (bulk material) XRD (ICDD 01-088-0826)	2.3874	1.7866
A5	2.3479	1.7220
A10	2.3537	1.7391
A20	2.3697	1.7635
AH5	2.3495	1.7224
AH10	2.3552	1.7430
AH20	2.3725	1.7657

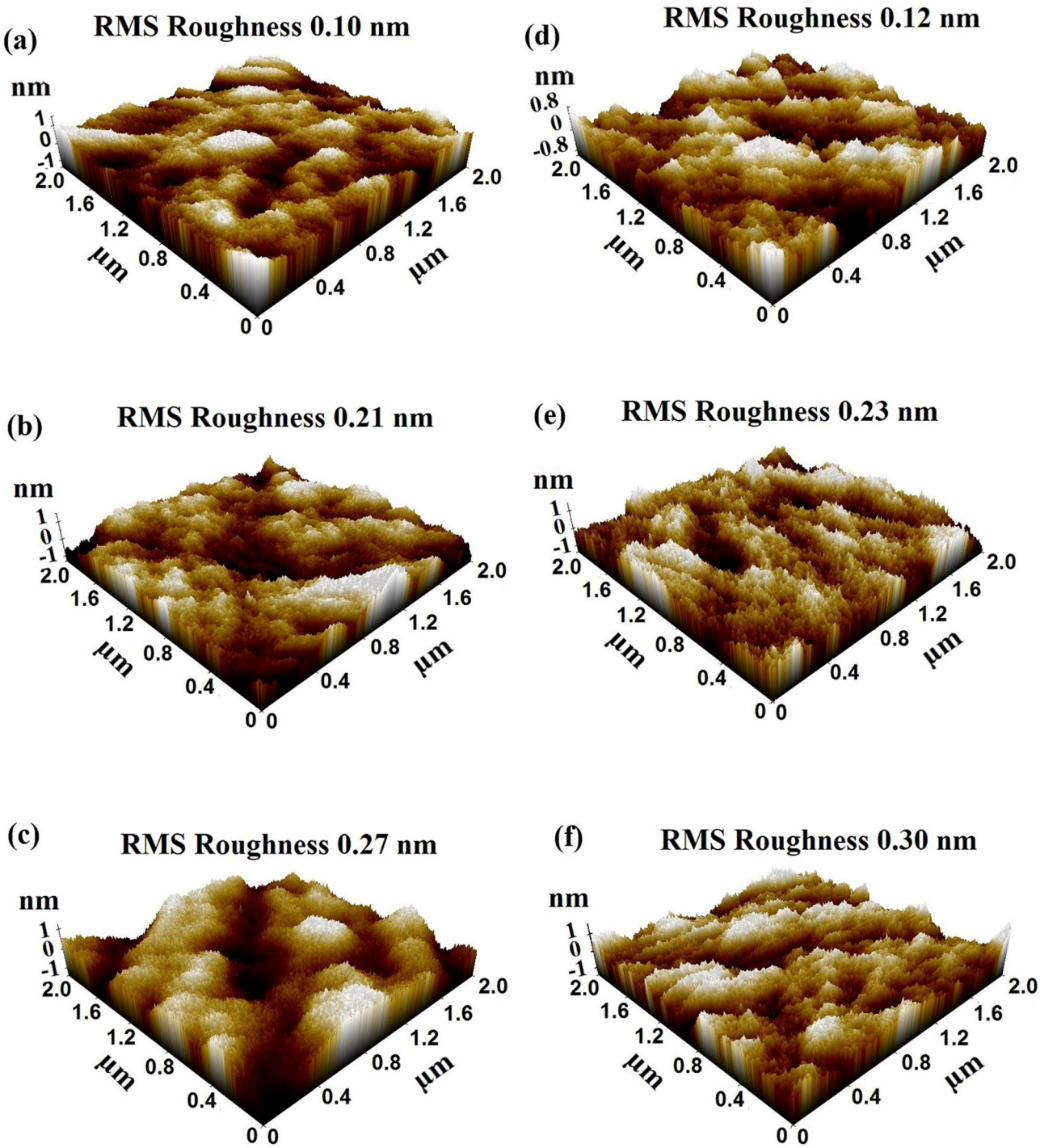

Fig. 2 AFM 3D images of deposited thin films: **a** A5, **b** A10, **c** A20, **d** AH5, **e** AH10 and **f** AH20

The optical properties were evaluated through reflectance spectra and Tauc plots. The reflectance spectra of all Al_2O_3 and $Al_{1.997}Hf_{0.003}O_3$ thin films are presented in Fig. 4a and b, respectively. Figure 5a and b shows the corresponding Tauc plots of all thin films. The bandgap energies are obtained using the Tauc plots according to the method given by Kamarulzaman et al. [26]. The obtained absorption edges and bandgap energies of all the Al_2O_3 and $Al_{1.997}Hf_{0.003}O_3$ films are listed in Table 3. For all Al_2O_3 thin films, the bandgap energies obtained are 5.81 eV to 5.96 eV. In contrast, the bandgap energies

Table 2 Root mean square (Rq) roughness of deposited thin films

Thin film	Rq roughness (nm)
A5	0.10
A10	0.21
A20	0.27
AH5	0.12
AH10	0.23
AH20	0.30

obtained for all $Al_{1.997}Hf_{0.003}O_3$ thin films are 5.26 eV to 5.64 eV. It is observed that the thinner the film, the larger is their bandgap energy. The thinner samples have larger bandgaps attributable to the quantum confinement effect of low dimensional structures [31]. In very thin films, atoms are more likely to reside on the surface of the thin films which will increase the density of unsaturated bonds. These bonds are identified as dangling bonds that cause defects in thinner films. Defects create localized states in the films and in this case, the width of energy gaps will be increased in thinner films. Consequently, overlapping energy levels spread out to become more quantized producing bandgap widening for thinner films that is comparable to the effects of nanoscale powders. In comparison, it is found that bandgap value of these results are higher than the HfO_2 thin films for reasonably similar gate oxide thickness as also reported by Jin et al. [36].

To evaluate the gate dielectric properties of the films, MOS capacitors of Pt/Al_2O_3/p-Si and Pt/$Al_{1.997}Hf_{0.003}O_3$/p-Si of different oxide thickness was fabricated. As shown in Fig. 6, the schematic circuit structure forms the Ohmic contact for *I–V* and *C–V* measurements. The corresponding *I–V* characteristics are shown in Fig. 7 which shows all the *I–V* characteristics of A5, A10, A20, AH5, AH10 and AH20 samples. The physical parameters of all films are listed in Table 4. It is observed that all samples exhibit rectifying behaviour. From the characteristics, it is perceived that within the threshold voltages, $V_t \leq V \leq V_{t'}$, for both forward and reverse bias, respectively, the values of the current are zero.

Throughout forward bias, the turn-on voltage, V_o, increase with film thickness, while the bandgap decreases. In the forward bias, there is a threshold voltage, V_t, whereby the current starts to be non-zero when the voltage is increased. This is known to be the minimum energy required for the electrons to tunnel out through the potential barrier and due to this, V_t will be termed the tunnelling voltage. The increase of the tunnelling voltage with decreasing bandgap is unpredicted and can only be elucidated by quantum theory. Rationally, the threshold and the turn-on voltages of higher bandgap films should be greater in value than lower bandgap films. However, this is not the case, but the phenomenon has been observed earlier by Kamarulzaman et al. [31]. They observed that the phenomenon is attributed to the quantum tunnelling effect observed with nanodimensional structures. This effect allows electrons to tunnel through the potential barrier. This phenomenon explains the movement of a particle passes through a potential barrier where it is impossible for it to surmount in classical view. The barrier is known as the bandgap, E_g, of the thin film. Figure 8 explains the quantum tunnelling phenomenon, whereby electrons with lower energy can tunnel out in thinner films even though the bandgap is higher. Therefore, evidently, at the nanoscale, the thinner the film, and the higher is the bandgap implying higher barrier height, and that it is easier for the electrons to surmount a higher potential barrier if the physical dimensions of the thin films are very small. Consequently, in nanoscale, thinner films with higher bandgaps exhibit lower threshold and turn-on voltages compared to thicker films with lower bandgaps and the results are listed in Table 4. The electron energies given in Table 4 are determined using Eq. (1). To further explain the effect of quantum tunnelling, studies toward the leakage current density, *J*, were done.

$$E_e = eV_t \quad (1)$$

The leakage current density, *J*, of the fabricated MOS capacitor with A5, A10, A20, AH5, AH10 and AH20 thin film samples are measured with respect to voltage, *V*, under the bias voltage range from – 4 V to 4 V. Figure 9a and b shows the *J–V* curves of Pt/Al_2O_3/p-Si and Pt/$Al_{1.997}Hf_{0.003}O_3$/p-Si MOS capacitors, respectively. All thin films possess leakage current density in the range of 10^{-10} to 10^{-7} A/cm^2 at 1 V as listed in Table 4. It is observed that, the leakage current density of Pt/Al_2O_3/p-Si and Pt/$Al_{1.997}Hf_{0.003}O_3$/p-Si differs only by one order of magnitude for the similar thickness of films. The results show that the thinner the film the higher the leakage current. This is as expected due to the quantum tunnelling effect discussed previously,

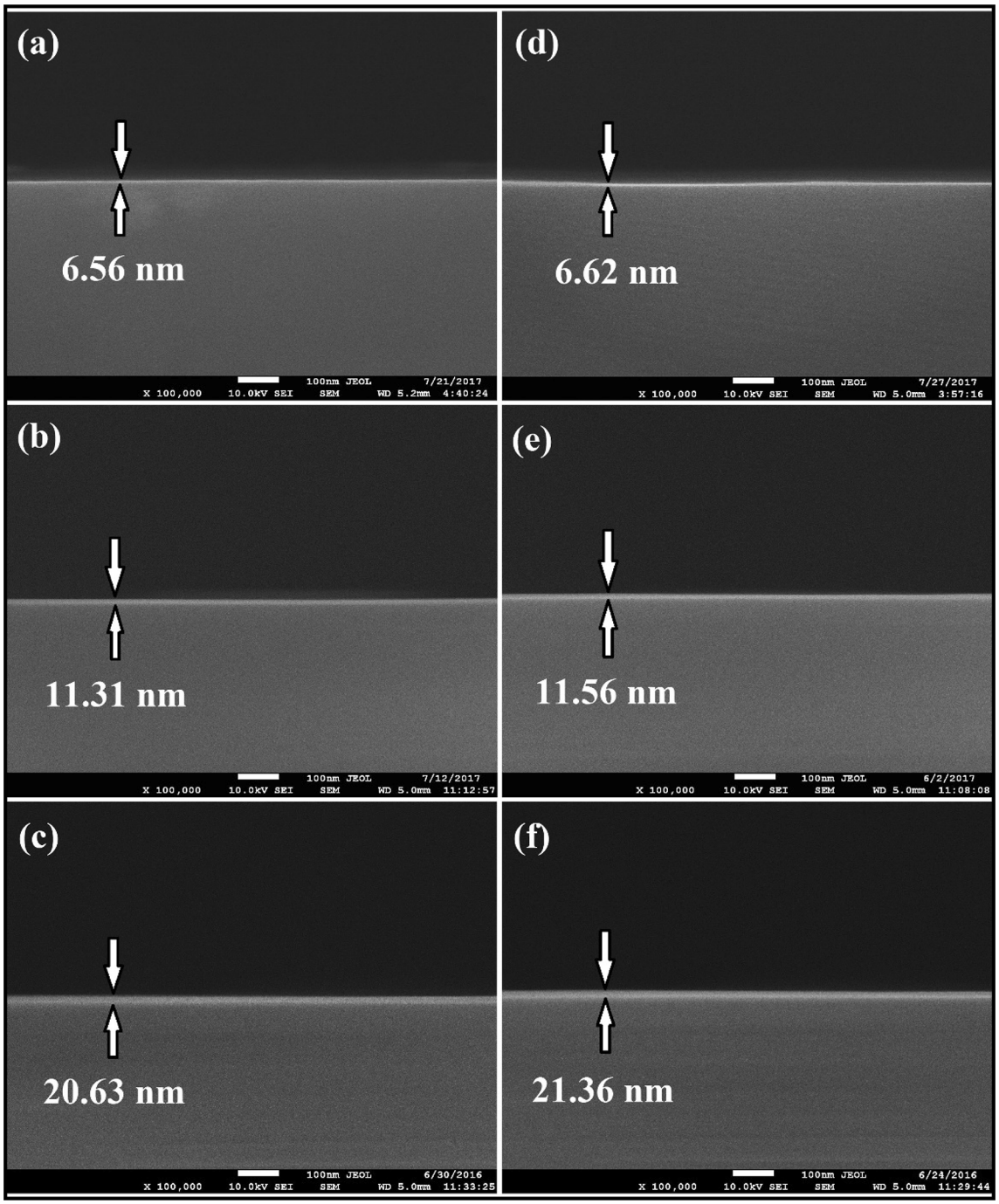

Fig. 3 SEM cross-section images for Al_2O_3 and $Al_{1.997}Hf_{0.003}O_3$: **a** A5, **b** A10, **c** A20, **d** AH5, **e** AH10 and **f** AH20

whereby more electrons with lower energy can tunnel out in thinner films. It is observed that the novel $Al_{1.997}Hf_{0.003}O_3$ thin films possess lower leakage current density than Al_2O_3 thin films by one order of magnitude. This is attributed to the thicker film of the AH5, AH10 and AH20 compared to A5, A10 and A20, respectively. Thicker films reduce the possibility of electron tunnelling and improve leakage current density. It is found that the leakage current densities in this work are two orders of magnitude lower with HfO_2. These findings agree with that reported by Wang et al. [37].

The *C–V* measurements of the fabricated MOS devices are measured at the frequency of 1 MHz at

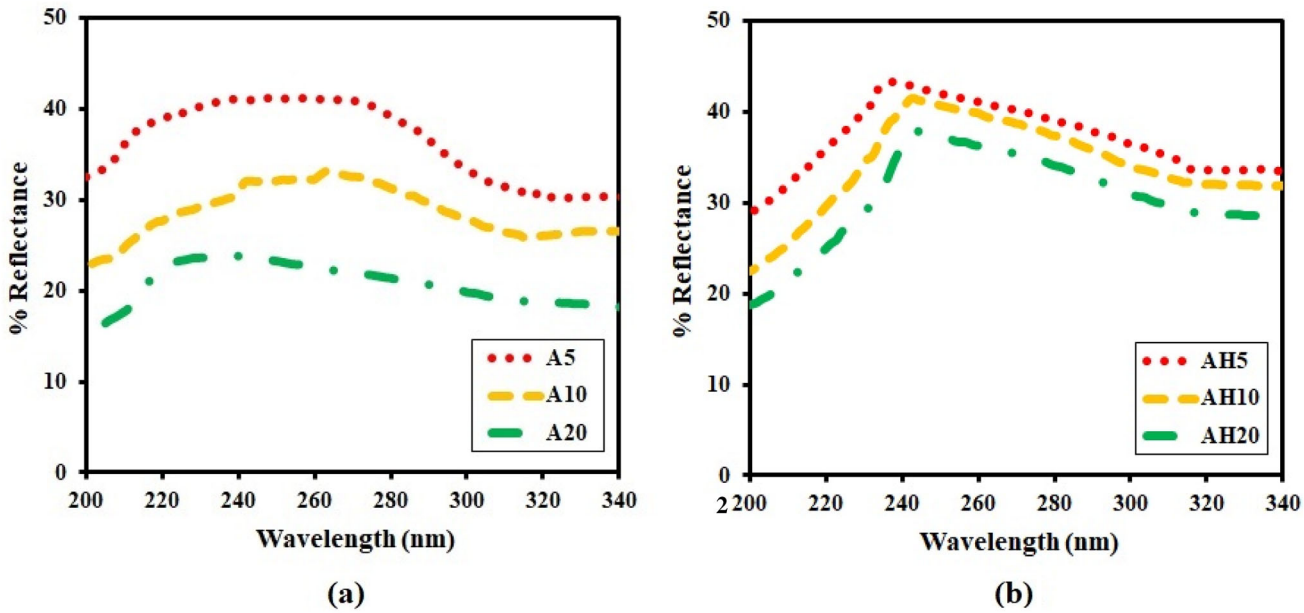

Fig. 4 **a** Reflectance spectra of all Al_2O_3 thin films and **b** reflectance spectra of all $Al_{0.997}Hf_{0.003}O_3$ thin films

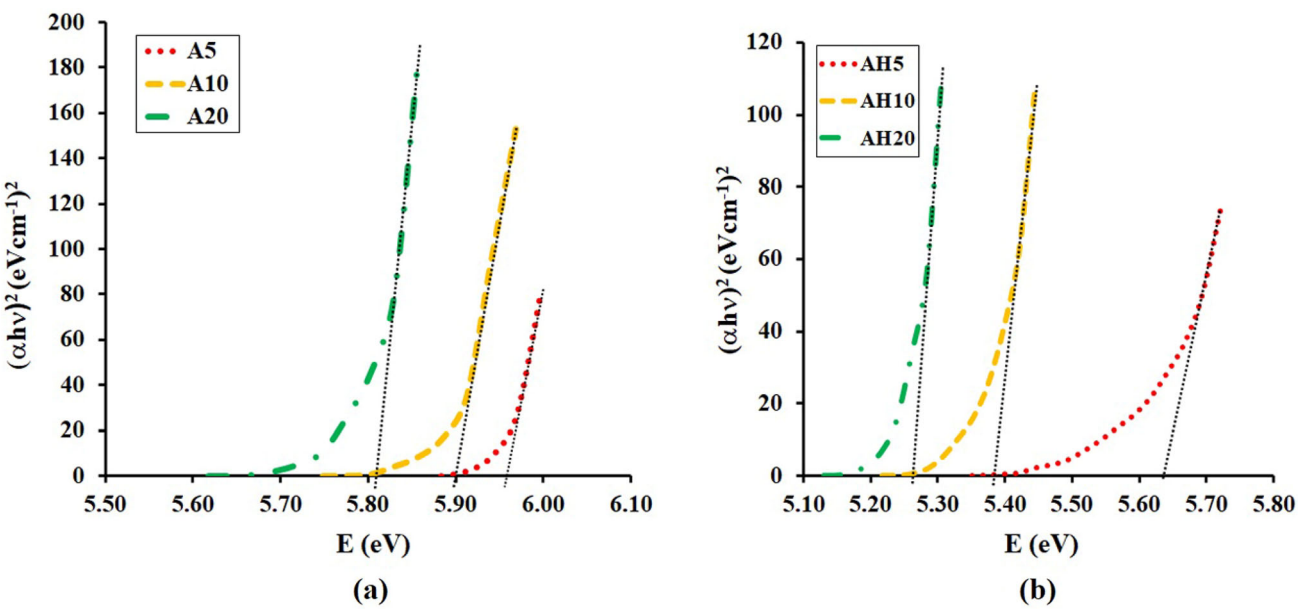

Fig. 5 **a** Tauc plots for all Al_2O_3 thin films and **b** Tauc plots of all $Al_{1.997}Hf_{0.003}O_3$ thin films

Table 3 Absorption edge and bandgap energy of All Al_2O_3 and $Al_{1.997}Hf_{0.003}O_3$ thin films

Sample	Thickness (nm)	Absorption edge (nm)	Bandgap energy ± 0.01 (eV)
A5	6.56	205	5.96
A10	11.31	209	5.90
A20	20.63	211	5.81
AH5	6.62	213	5.64
AH10	11.56	226	5.38
AH20	21.36	232	5.26

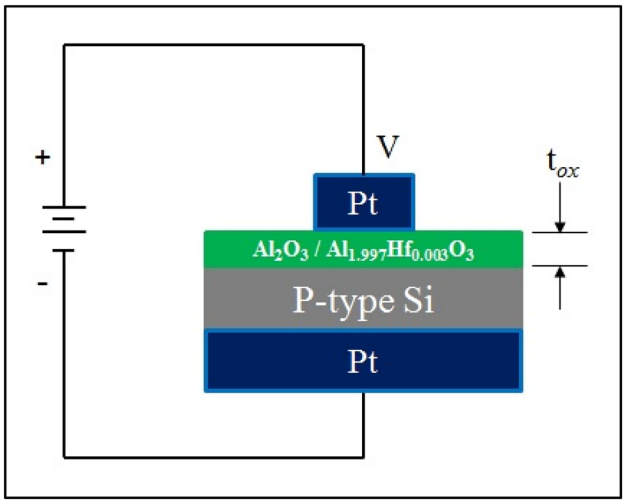

Fig. 6 Circuit test structure of the fabricated MOS capacitor

applied bias − 4 V to 4 V. Figure 10a and b shows the *C*–*V* characteristic curves of different thicknesses for Pt/Al_2O_3/p-Si and Pt/$Al_{1.997}Hf_{0.003}O_3$/p-Si MOS capacitors, respectively. From the figures, all MOS capacitor at different oxide thicknesses show typical p-type behaviour with clear accumulation, depletion, and inversion regions. When the applied negative gate voltage is lower than the flat-band voltage ($V < V_{FB}$) it induces negative charges on the metal gate and positive charge in the semiconductor. Positively charged holes are attracted toward the substrate surface; hence, the MOS capacitor starts to store positive charge at the substrate surface. This condition is called accumulation. In the accumulation region, the MOS capacitor is just a simple capacitor with capacitance, C_{ox} of the particular oxide [38–40]. Hence, from the results, the capacitance values of Al_2O_3 and $Al_{1.997}Hf_{0.003}O_3$ films are identified at the accumulated capacitance region as can be seen in the *C*–*V* plot and are listed in Table 5.

Obviously, the accumulated capacitances are highly affected by the scaling of the gate oxide thickness. For both Pt/Al_2O_3/p-Si and Pt/$Al_{1.997}Hf_{0.003}O_3$/p-Si MOS capacitors, as the thickness of gate oxide increase, the capacitance decreases. This trend is similar to other reports [41–43]. In comparison, Pt/$Al_{1.997}Hf_{0.003}O_3$/p-Si exhibit higher capacitance than Pt/Al_2O_3/p-Si at all thicknesses. This is because $Al_{1.997}Hf_{0.003}O_3$ possess higher *k*, than Al_2O_3. The bandgaps of $Al_{1.997}Hf_{0.003}O_3$ thin films also agree well with the result of *k* value where all the bandgaps of $Al_{1.997}Hf_{0.003}O_3$ thin films possess lower values compared to Al_2O_3 thin films. This is very true in accordance with Robertson [44], where the *k* of gate oxides tends to vary inversely with the bandgap. The *k* value of the gate oxide at different thicknesses are calculated using Eq. (2) and are listed in Table 5.

$$k = \frac{C_{ox} t_{ox}}{\epsilon_o A} \tag{2}$$

In an ideal MOS capacitor, the condition of flat-band voltage V_{FB}, occurs when $V = 0$, it means that no charge exists on the plates of the capacitor. However, for a non-ideal capacitor, its numerical value depends on the doping of the capacitor and on any residual interface charge that may exist at the interface between the semiconductor and the insulator. From the accumulated capacitance, C_{ox}, the accumulated charge, Q_{Acc}, at the semiconductor-oxide interface are obtained by Eq. (3) [38, 39],

$$|Q_{Acc}| = -C_{ox}(V - V_{FB}) \tag{3}$$

From Eq. (3), a plot of accumulated charge, $|Q_{Acc}|$ as a function of the applied voltage, *V* can be drawn. The point of the extrapolation of the linear part that meets the abscissa will give the value of V_{FB} of the MOS capacitor. Figure 11a and b shows the plots of accumulated charge, $|Q_{Acc}|$ as a function of the applied voltage, *V* for Pt/Al_2O_3/p-Si and Pt/$Al_{1.997}Hf_{0.003}O_3$/p-Si MOS capacitors, respectively. The values of V_{FB} are given in Table 5. The shift in *C*–*V* curve indicates the presence of positive oxide charges at the oxide–semiconductor interface [38, 45]. It is observed that the small shifts (toward negative voltage) are increased for decreasing *k* values for both Pt/Al_2O_3/p-Si and Pt/$Al_{1.997}Hf_{0.003}O_3$/p-Si MOS capacitors. The results are very well agreed with Maity et al. [43] where it is observed that the V_{FB} approaches to zero for greater dielectric constant. Likewise, all curves are near to the ideal condition ($V_{FB} = 0$) which is a good testament showing that the thin films are very well form as supported from the structural and morphology results.

4 Conclusions

High-quality, uniform and smooth $Al_{1.997}Hf_{0.003}O_3$ thin films were deposited by PLD. It was found that the number of laser pulses and chamber environments influence the characteristics of the deposited thin films. The thin films formed were of the

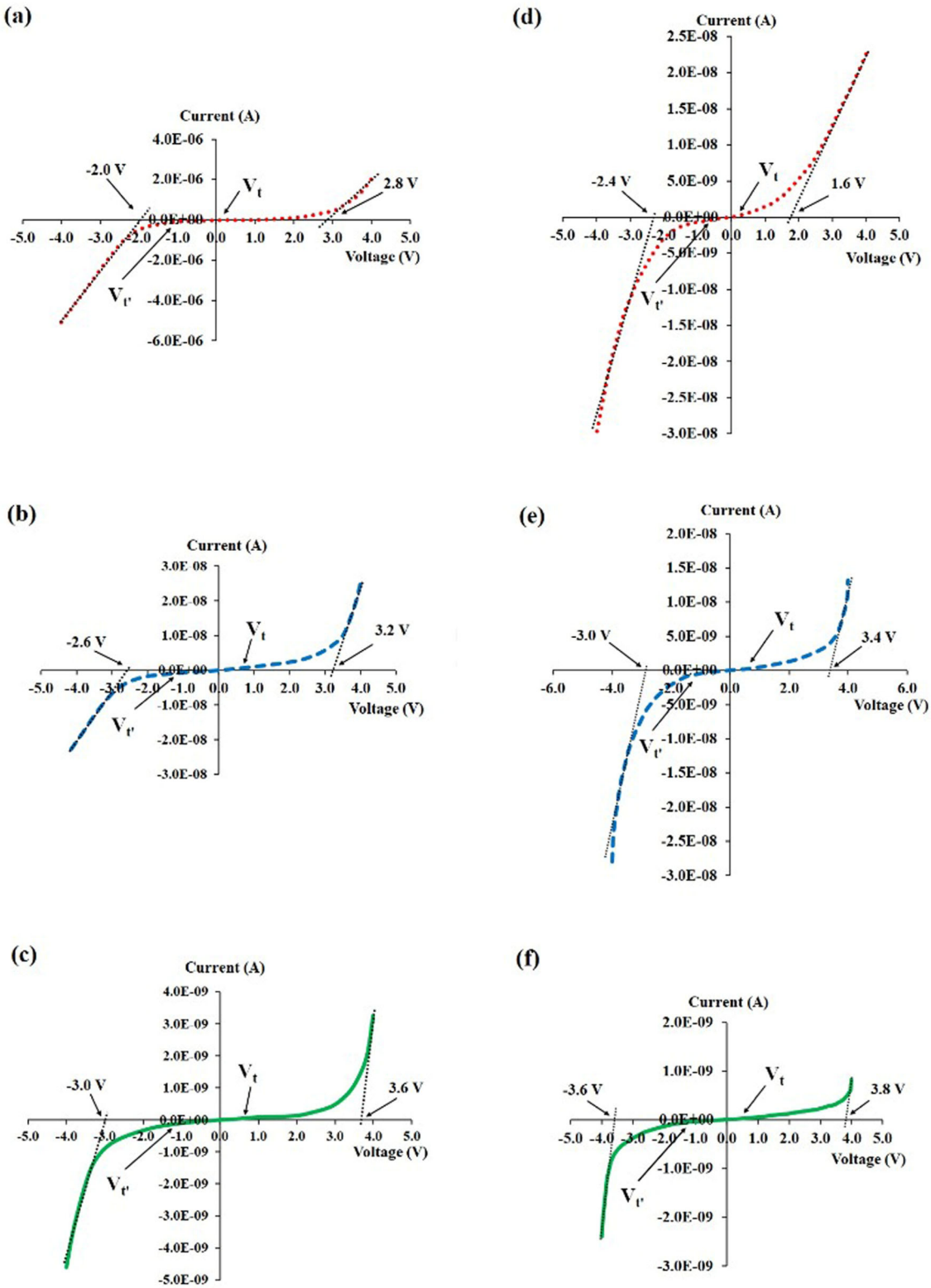

Fig. 7 *I–V* curves of **a** A5, **b** A10, **c** A20, **d** AH5, **e** AH10, and **f** AH20 thin films

stable hexagonal crystal structure as the compacted source targets were prepared from the highly stable pre-synthesized powders of the hexagonal crystal structure. It was observed that the thinner the

Table 4 Parameters of Al_2O_3 and $Al_{1.997}Hf_{0.003}O_3$ thin films and their *I–V* characteristics

Sample	Thickness (nm)	Bandgap, E_g (eV)	Breakdown voltage, V_b (V)	Threshold voltage in reverse bias, $V_{t'}$ (V)	Turn-On voltage, V_o (V)	Threshold voltage in forward bias, V_t (V)	Tunnelling electron energy, E_e (eV)	Leakage current, J at 1 V (A/cm^2)
A5	6.56	5.96	− 2.0	− 0.9	2.8	0.4	0.4	3.10×10^{-7}
A10	11.31	5.90	− 2.6	− 0.8	3.2	0.6	0.6	1.41×10^{-8}
A20	20.63	5.81	− 3.0	− 1.0	3.6	0.8	0.8	1.19×10^{-9}
AH5	6.62	5.64	− 2.4	− 0.6	1.6	0.2	0.2	1.53×10^{-8}
AH10	11.56	5.38	− 3.0	− 1.0	3.4	0.6	0.6	6.30×10^{-9}
AH20	21.36	5.26	− 3.6	− 1.4	3.8	0.8	0.8	8.87×10^{-10}

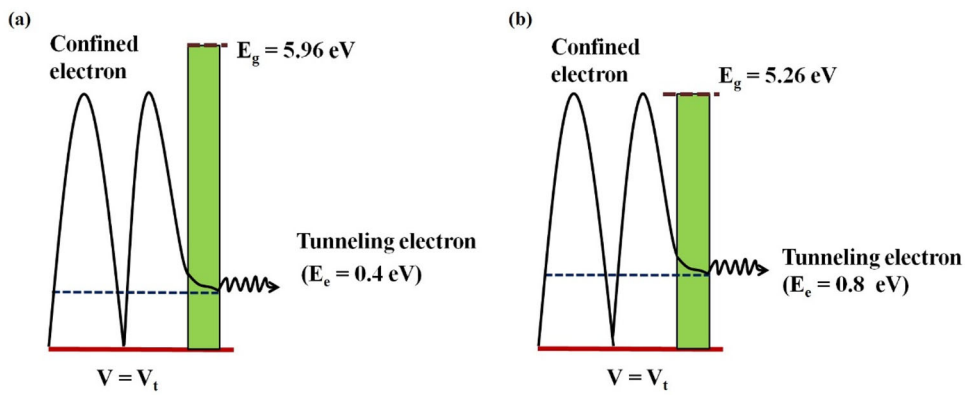

Fig. 8 Illustration of the quantum tunnelling effects showing the electron wave in **a** thinner Al_2O_3 film (A5 sample) and **b** thicker $Al_{1.997}Hf_{0.003}O_3$ film (AH20 sample)

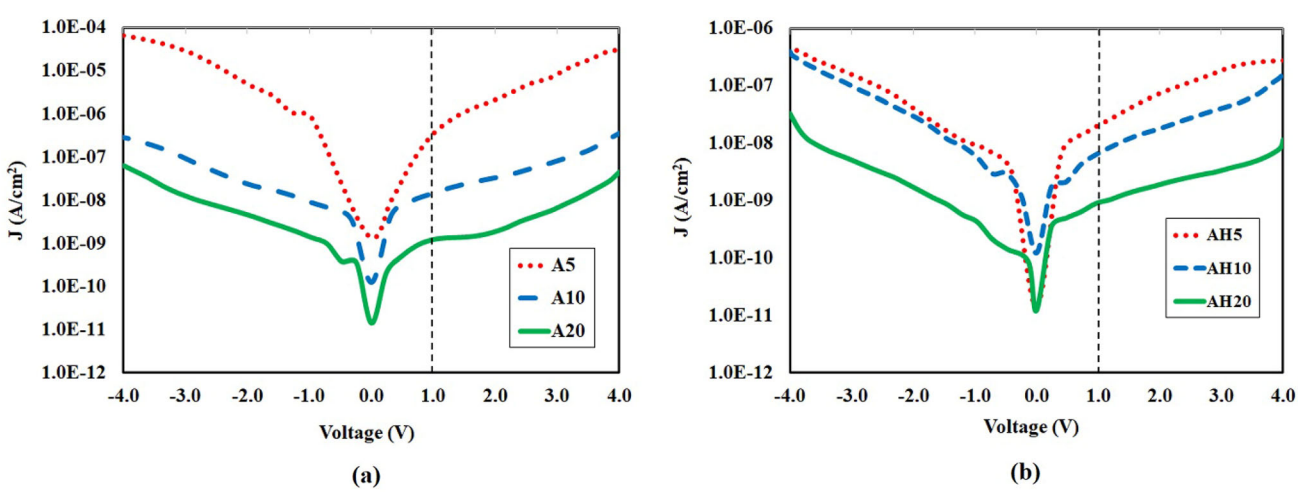

Fig. 9 **a** Leakage current density of Al_2O_3 thin films and **b** leakage current density of $Al_{1.997}Hf_{0.003}O_3$ thin films

film, the larger was their bandgap energy. The thinner films have larger bandgaps attributable to the quantum confinement effect of low dimensional structures, where more atoms residing on the surface of the thin films hence increases the density of unsaturated bonds. Pt/Al_2O_3/p-Si and Pt/$Al_{2-x}Hf_xO_3$/p-Si MOS capacitors were fabricated to show the significance and suitability of $Al_{1.997}Hf_{0.003}O_3$ high-*k* gate dielectric thin film for next generation MOS devices. Experimental results demonstrating lower threshold and turn-on voltages as well as higher leakage current for thinner films with higher bandgaps are evidence of quantum tunnelling occurring in nanodimensional structures. The capacitances of the

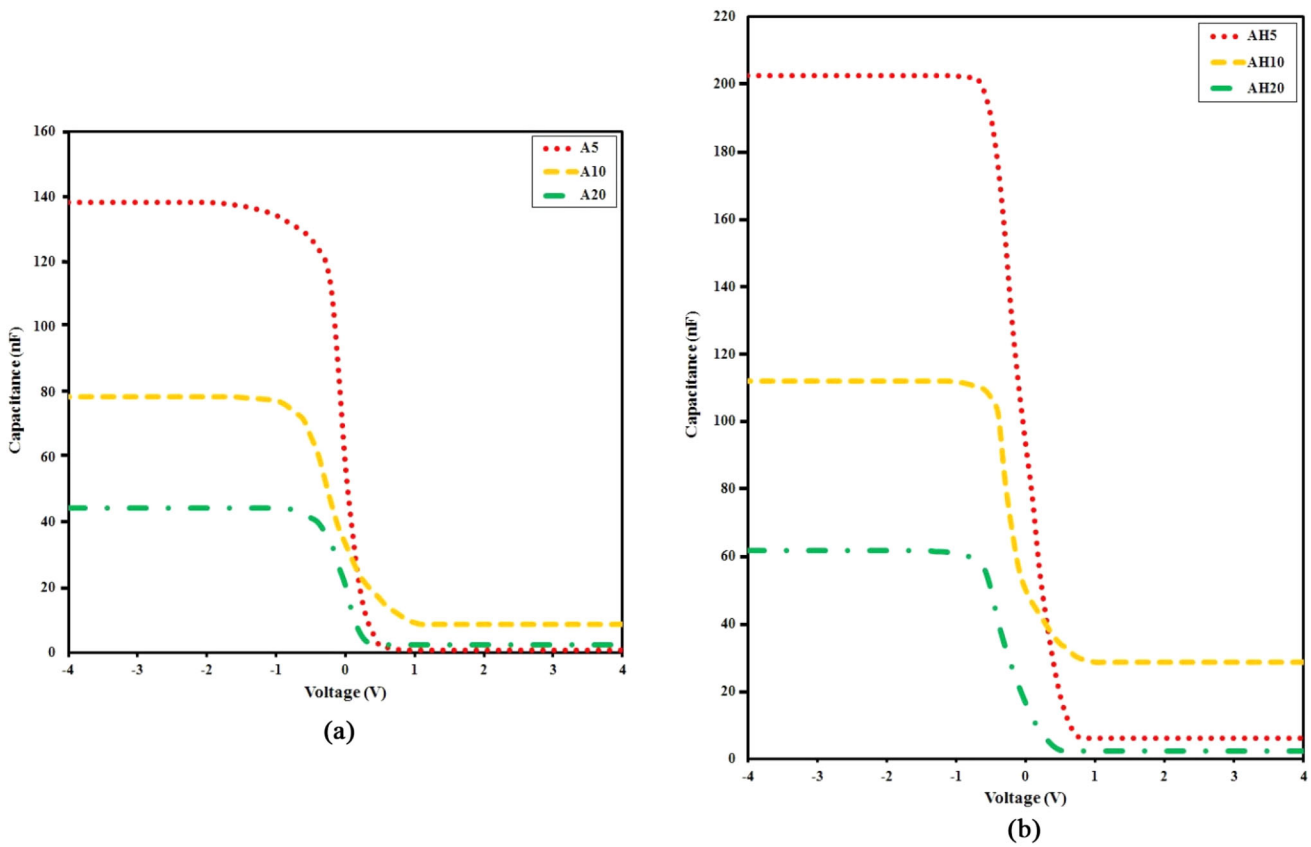

Fig. 10 **a** *C–V* characteristics of Pt/Al_2O_3/P-Si MOS capacitors at different oxide thicknesses measured at 1 MHz and **b** *C–V* characteristics of Pt/$Al_{1.997}Hf_{0.003}O_3$/P-Si MOS capacitors at different oxide thicknesses measured at 1 MHz

Table 5 Oxide thickness (t_{ox}), bandgap (E_g), gate oxide capacitance (C_{ox}), dielectric constant (k) and flat-band voltage (V_{FB}) of all samples extracted from 1 MHz *C–V* curves

Sample	Thickness (nm)	Bandgap, E_g(eV)	Gate oxide capacitance, C_{ox} (nF)	Dielectric constant, k	Flat-band voltage, V_{FB} (V)
A5	6.56	5.96	138.21	14.21	− 0.20
A10	11.31	5.90	78.54	14.27	− 0.15
A20	20.63	5.81	44.30	14.54	− 0.10
AH5	6.62	5.64	202.56	21.18	− 0.30
AH10	11.56	5.38	111.85	21.39	− 0.20
AH20	21.36	5.26	59.69	21.46	− 0.10

fabricated MOS capacitors were highly affected by the scaling of the gate oxide thickness. The capacitance decreases as the thickness of gate oxide increases. The inclusion of Hf into Al_2O_3 had significantly increased the k value. Consequently, Pt/$Al_{1.997}Hf_{0.003}O_3$/p-Si exhibit higher capacitance than Pt/Al_2O_3/p-Si. According to these results, $Al_{1.997}Hf_{0.003}O_3$ thin films that have been developed in this work could be significant in the search for a replacement gate dielectric for future MOS devices.

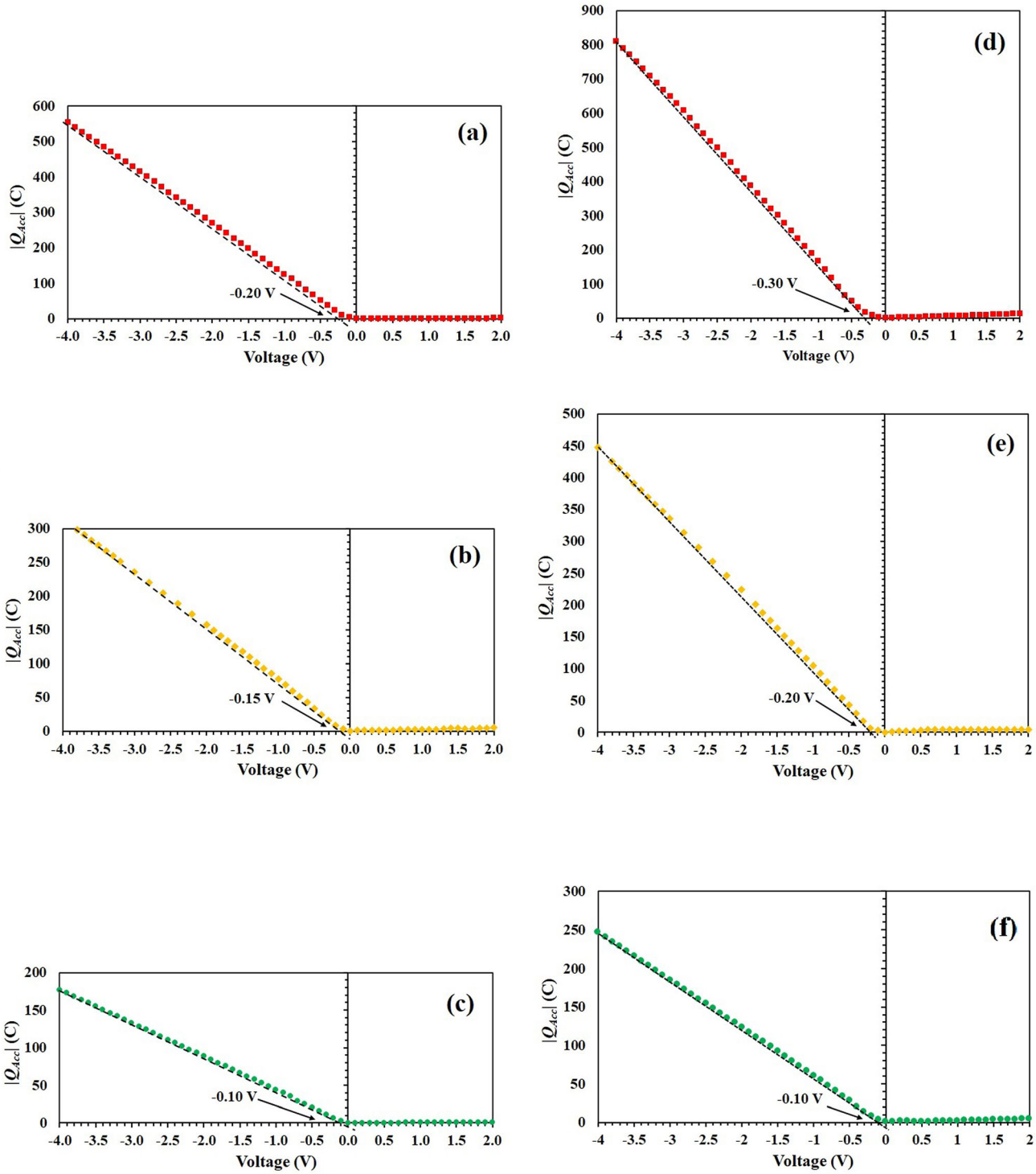

Fig. 11 Accumulated charge, $|Q_{Acc}|$, as a function of the applied voltage, V **a** A5, **b** A10, **c** A20, **d** AH5, **e** AH10 and **f** AH20

Acknowledgements

The authors would like to express their gratitude to the Institute of Science, Faculty of Applied Sciences and Research Management Centre (RMC) of Universiti Teknologi MARA for assistance and internal funding of the study. This study was financially supported by the Universiti Teknologi MARA under Special Research Grant No. 600-RMC/GPK 5/3 (140/2020).

Declarations

Conflict of interest The authors certify that they have NO affiliations with or involvement in any organization or entity with any financial interest (such as honoraria; educational grants; participation in speakers' bureaus; membership, employment, consultancies, stock ownership, or other equity interest; and expert testimony or patent-licensing arrangements), or non-financial interest (such as personal or professional relationships, affiliations, knowledge or beliefs) in the subject matter or materials discussed in this manuscript.

References

1. R. Williams, Photoemission of electrons from silicon into silicon dioxide. Phys. Rev. **140**, 569 (1965)
2. S. Toyoda, M. Oshima, Thickness-dependent change in the valence band offset of the SiO_2/Si interface studied using synchrotron-radiation photoemission spectroscopy. J. Appl. Phys. (2016). https://doi.org/10.1063/1.4961220
3. K.K. Hung, Y.C. Cheng, Characterization of Si SiO_2 interface traps in metal oxide semiconductor structures with thin oxides by conductance technique structures with thin oxides by conductance technique. J. Appl. Phys. (2013). https://doi.org/10.1063/1.339091
4. T.C. Leung et al., Study of SiO_2 Si and metal oxide semiconductor structures using positrons Study of SiO_2–Si and metal-oxide-semiconductor using positrons. J. Appl. Phys (1996). https://doi.org/10.1063/1.353879
5. S. Iwata, A. Ishizaka, Electron spectroscopic analysis of the SiO_2/Si system and correlation with metal-oxide-semiconductor device characteristics. J. Appl. Phys. (1996). https://doi.org/10.1063/1.362676
6. D. Schmidt et al., New approach to preparing smooth Si (100) surfaces: characterizationby spectroellipsometry and validation of Si/SiO_2 interfacesproperties in metal-oxide-semiconductor devices. J. Vac. Sci. Technol. B Microelectron. Nanometer Struct. Process. Meas. Phenom. (1996). https://doi.org/10.1116/1.588838
7. M.L. Green et al., Understanding the limits of ultrathin SiO_2 and Si–O–N gate dielectrics for sub-50 nm CMOS. Microelectron. Eng. **48**, 25–30 (1999). https://doi.org/10.1016/S0167-9317(99)00330-5
8. K. Komiya, Y. Omura, Spectroscopic characterization of stress-induced leakage current in sub 5-nm-thick silicon oxide film. J. Appl Phys. (2007). https://doi.org/10.1063/1.1499978
9. P. Tseng, J. Hwu, Non-planar substrate effect on the interface trap capacitance of metal-oxide-semiconductor structures with ultra thin oxides. J. Appl. Phys. (2014). https://doi.org/10.1063/1.4761972
10. M. Hirose, M. Koh, W. Mizubayashi, H. Murakami, K. Shibahara, S. Miyazaki, Fundamental limit of gate oxide thickness scaling in advanced MOSFETs. Semicond. Sci. Technol. **15**, 485–490 (2000). https://doi.org/10.1088/0268-1242/15/5/308
11. H.H. Radamson et al., The challenges of advanced CMOS process from 2D to 3D. Appl. Sci. **7**, 10 (2017). https://doi.org/10.3390/app7101047
12. S.H. Lo, D.A. Buchanan, Y. Taur, W. Wang, Quantum-mechanical modeling of electron tunneling current from the inversion layer of ultra-thin-oxide nMOSFET's. IEEE Electron. Device Lett. **18**(5), 209–211 (1997). https://doi.org/10.1109/55.568766
13. Z.A. Weinberg, On tunneling in metal oxide silicon structures. J. Appl. Phys. **53**(7), 5052–5056 (1982). https://doi.org/10.1063/1.331336
14. J.M.A. G.Wilk, R.M. Wallace, High-κ gate dielectrics: current status and materials properties considerations. J. Appl. Phys. **89**(10), 5243 (2001)
15. H. Sasaki, H. Ono, M. Yoshitomi, T. Ohguro, T. Nakamura, S. Saito, Iwai, 1.5 nm direct-tunneling gate oxide Si MOSFET's. IEEE Trans. Electron. Devices **43**(8), 1233–1242 (1996). https://doi.org/10.1109/16.506774
16. H.H. Radamson et al., State of the art and future perspectives in advanced CMOS technology. Nanomaterials **10**, 1–86 (2020). https://doi.org/10.3390/nano10081555
17. P. Vitanov, A. Harizanova, T. Ivanova, C. Trapalis, N. Todorova, Sol–gel ZrO_2 and ZrO_2–Al_2O_3 nanocrystalline thin films on Si as high-k dielectrics. Mater. Sci. Eng. B Solid-State Mater. Adv. Technol. **165**(3), 178–181 (2009). https://doi.org/10.1016/j.mseb.2009.09.002
18. R. Sohal, G. Lupina, O. Seifarth, P. Zaumseil, C. Walczyk, T. Schroeder, Improving the dielectric constant of Al_2O_3 by cerium substitution for high-k MIM applications. Surf. Sci. **604**, 3–4 (2010). https://doi.org/10.1016/j.susc.2009.11.017
19. J. Robertson, R.M. Wallace, High-K materials and metal gates for CMOS applications. Mater. Sci. Eng. R Rep. (2015). https://doi.org/10.1016/j.mser.2014.11.0012014.11.001
20. J. Robertson, B. Falabretti, Band offsets of high K gate oxides on high mobility semiconductors. Mater. Sci. Eng. B **135**(3), 267–271 (2006). https://doi.org/10.1016/j.mseb.2006.08.017
21. J. Robertson, Band offsets of high dielectric constant gate oxides on silicon. J. Non Cryst. Solids **303**(1), 94–100 (2002). https://doi.org/10.1016/S0022-3093(02)00972-9
22. H. Padma Kumar, S. Vidya, S. Saravana Kumar, C. Vijayakumar, S. Solomon, J.K. Thomas, Optical properties of

nanocrystalline HfO_2 synthesized by an auto-igniting combustion synthesis. J. Asian Ceram. Soc. **3**(1), 64–69 (2015). https://doi.org/10.1016/j.jascer.2014.10.009

23. B.H. Lee, L. Kang, R. Nieh, W.-J. Qi, J.C. Lee, Thermal stability and electrical characteristics of ultrathin hafnium oxide gate dielectric reoxidized with rapid thermal annealing. Appl. Phys. Lett. **76**(14), 192 (2000)
24. Y. Wang et al., Improved thermal stability, interface, and electrical properties of HfO_2 films prepared by pulsed laser deposition using in situ ionized nitrogen. Appl. Phys. Lett. **95**(3), 032905 (2009). https://doi.org/10.1063/1.3184577
25. T. Tan, Z. Liu, H. Lu, W. Liu, H. Tian, Structure and optical properties of HfO2 thin films on silicon after rapid thermal annealing. Opt. Mater. (Amst) **32**(3), 432–435 (2010). https://doi.org/10.1016/j.optmat.2009.10.003
26. N. Kamarulzaman, A.M. Mahat, N. Badar, C.Z. Zhao, Structural and band gaps studies of novel $Al_{2-x}Hf_xO_3$ materials toward MOS applications. Mater. Chem. Phys. **216**, 237–242 (2018). https://doi.org/10.1016/j.matchemphys.2018.03.093
27. A.M. Mahat, N. Kamarulzaman, M.S. Mastuli, N. Badar, N.A. Jani, M.F. Omar, Mechanism of the formation of novel $Al_{2-x}Hf_xO_3$ materials via a combustion synthesis method. Results Mater. **6**, 100075 (2020). https://doi.org/10.1016/j.rinma.2020.100075
28. C. Belouet, Thin film growth by the pulsed laser assisted deposition technique. Appl. Surf. Sci. **96–98**, 630–642 (1996). https://doi.org/10.1016/0169-4332(95)00535-8
29. J.L. Zhao, X.M. Li, J.M. Bian, W.D. Yu, X.D. Gao, Structural, optical and electrical properties of ZnO films grown by pulsed laser deposition (PLD). J. Cryst. Growth **276**, 3–4 (2005). https://doi.org/10.1016/j.jcrysgro.2004.11.407
30. K. Yang, B. Li, G. Zeng, Sb_2Se_3 thin film solar cells prepared by pulsed laser deposition. J. Alloys Compd. **821**, 153505 (2020). https://doi.org/10.1016/j.jallcom.2019.153505
31. N. Kamarulzaman, N. Badar, N.F. Chayed, M.F. Kasim, Band gap widening and quantum tunnelling effects of Ag/MgO/p-Si MOS structure. Mater. Res. Express **3**(10), 106401 (2016). https://doi.org/10.1088/2053-1591/3/10/106401
32. G. Wang, O. Marty, C. Garapon, A. Pillonnet, W. Zhang, Rare earth doped α-alumina thin films prepared by pulsed laser deposition: structural and optical properties. Appl. Phys. A **79**, 4–6 (2004). https://doi.org/10.1007/s00339-004-2859-8
33. J. Gao et al., Microstructure, wettability, optical and electrical properties of HfO_2 thin films: effect of oxygen partial pressure. J. Alloys Compd. **662**, 339–347 (2016). https://doi.org/10.1016/j.jallcom.2015.12.080
34. K. Badar, N. Kamarulzaman, N. Mahat, A.M. Chayed, Elong, Studies on the characteristics and the effect of thickness on the band gap energies of Al_2O_3 thin films prepared by PLD. Solid State Phenom. **290**, 163–167 (2019). https://doi.org/10.4028/www.scientific.net/SSP.290.163
35. X. Xiang, L. Zhu, F. Yang, L. Hu, G. Zhang, Fe effect on hydrogen interactions with intrinsic point defects and hydrogen migration in α-Al_2O_3 based tritium permeation barriers. J. Nuclear Mater. **542**, 152494 (2020)
36. P. Jin et al., Microstructure, optical, electrical properties, and leakage current transport mechanism of sol–gel-processed high-k HfO_2 gate dielectrics. Ceram. Int. **42**(6), 6761–6769 (2016). https://doi.org/10.1016/j.ceramint.2016.01.050
37. Y. Wang, H. Wang, C. Ye, J. Zhang, H. Wang, Y. Jiang, Interfacial reaction and electrical properties of HfO_2 film gate dielectric prepared by pulsed laser deposition in nitrogen: role of rapid thermal annealing and gate electrode. ACS Appl. Mater. Interfaces **3**(10), 3813–3818 (2011). https://doi.org/10.1021/am2008695
38. S.M. Sze, *Physics of Semiconductor Devices*, 3rd edn. (Wiley, Hoboken, 2007).
39. S.M. Sze, M.-K. Lee, *Semiconductor Devices: Physics and Technology* (Wiley, Singapore, 2013).
40. K. Adpakpang et al., Chemistry and physics of metal oxide nanostructures. J. Power Sources. (2015). https://doi.org/10.1038/nmat2749
41. J.H. Kim, V. Ignatova, P. Kücher, J. Heitmann, L. Oberbeck, U. Schröder, Physical and electrical characterization of high-k ZrO_2 metal-insulator-metal capacitor. Thin Solid Films **516**(23), 8333–8336 (2008). https://doi.org/10.1016/j.tsf.2008.03.051
42. Y. Choi, C.K. Song, Low leakage current through zirconium oxide gate fabricated by low temperature solution process in OTFTs on plastic substrate. Org. Electron. Phys. Mater. Appl. **52**, 195–199 (2018). https://doi.org/10.1016/j.orgel.2017.10.030
43. N.P. Maity, A. Kumar, R. Maity, S. Baishya, Analysis of flatband voltage for MOS devices using high-K dielectric materials. Procedia Mater. Sci. **5**, 1198–1204 (2014). https://doi.org/10.1016/j.mspro.2014.07.421
44. J. Robertson, High dielectric constant gate oxides for metal oxide Si transistors. Reports Prog. Phys. **69**(2), 327–396 (2006). https://doi.org/10.1088/0034-4885/69/2/R02
45. S. Addepalli, L.G. Kolla, U. Suda, Electrical, optical, structural and chemical properties of Al_2TiO_5 films for high-κ gate dielectric applications. Mater. Sci. Semicond. Process. **57**, 137–146 (2017). https://doi.org/10.1016/j.mssp.2016.10.019

Publisher's Note Springer Nature remains neutral with regard to jurisdictional claims in published maps and institutional affiliations.